Available online at www.sciencedirect.com
ScienceDirect
Computer Coupling of Phase Diagrams and Thermochemistry 31 (2007) 303–312
www.elsevier.com/locate/calphad

Thermodynamic description and growth kinetics of stoichiometric precipitates in the phase-field approach

S.Y. Hu[a,*], J. Murray[b], H. Weiland[b], Z.K. Liu[c], L.Q. Chen[c]

[a] *Los Alamos National Laboratory, MST8, Los Alamos, NM 87545, USA*
[b] *Alcoa Technical Center, 100 Technical Drive, Alcoa Center, PA 15069, USA*
[c] *Department of Material Science and Engineering, Penn State University, PA 16802, USA*

Received 20 January 2006; received in revised form 27 August 2006; accepted 27 August 2006
Available online 3 November 2006

Abstract

In theoretical analyses and computational simulations chemical free energies of stoichiometric compounds and solid solution phases are often approximated by parabolic functions. In the present work, we focus on examining the effect of different approximations of chemical free energies on predicted precipitate growth kinetics with phase-field modelling. As an example, we studied the precipitation of plate-like $\theta'(Al_2Cu)$ in Al–4 wt%Cu Alloys. Using six sets of chemical free energies for θ' and Al–Cu solid solution, growth kinetics of θ' precipitates were simulated by assuming either constant diffusivity or constant atomic mobility. It is demonstrated that the parabolic function provides a good description for the chemical free energy of a stoichiometric compound while the growth kinetics is sensitive to the approximation of chemical free energy for the solution phase.
Published by Elsevier Ltd

Keywords: Phase-field modelling; θ' precipitate; Growth kinetics; Al–Cu alloys

1. Introduction

Many intermetallic precipitates in which there is no solubility or the solubility is extremely small are known as 'line compounds'. The free energy of a line compound, by definition, is represented by a single value at a given temperature. Modelling the growth of stoichiometric line compounds via the phase-field approach poses serious numerical challenges since the derivative of the free energy does not exist. One possible approach is to approximate the free energy of a line compound by a parabolic function of composition. However, it is not clear how to choose the curvature and whether its magnitude has any significant effect on the predicted growth kinetics of a precipitate. Further, the free energy of a solution phase always contains an entropy mixing term. When the solute solubility is very low, e.g. at low temperatures, the logarithmic function term in the free energy function is also numerically challenging because numerical errors during temporal evolution may lead to negative values for the composition and thus blow-up of the logarithmic function. The main purpose of this paper is to examine the approximations for free energy functions of both a stoichiometric line compound and a solution phase on the predicted growth kinetics of a precipitate in a binary alloys in the context of phase-field modelling.

As an example, we consider precipitation of metastable $\theta'(Al_2Cu)$ phase, a stoichiometric line compound, in Al–Cu alloys. θ' is one of the primary strengthening precipitates in Al–Cu alloys [1–11]. This system is scientifically interesting as the precipitation process involves strong anisotropies of elastic interactions, interfacial energy and interface mobility. The phase-field approach has recently been employed to simulate the growth kinetics of this plate-like precipitate. Li and Chen [12] simulated stress-oriented nucleation and growth of θ' precipitates using two parabolic functions to describe the chemical free energies for θ' and α phases. Based on first-principles calculations, Vaithyanathan et al. [13] also constructed parabolic functions to describe chemical free energies of θ' and α phases, and studied the effect of elastic

* Corresponding author.
E-mail address: syhu@lanl.gov (S.Y. Hu).

0364-5916/$ - see front matter Published by Elsevier Ltd
doi:10.1016/j.calphad.2006.08.005

energy, interface energy anisotropy and interface mobility anisotropy on the morphology and growth of θ' precipitates.

In the present work, we extended Kim's model for solidification [14,15] to the precipitation reactions that involve strong anisotropies in interfacial energy and interface mobility, and we established relationships between model parameters and materials properties. One feature of this model is that the model parameter, interfacial energy coefficient, is uniquely determined by the interface thickness and interfacial energy, and is independent of chemical free energies. This feature allows one to study the effect of different approximations of chemical free energies on precipitate growth with one set of model parameters. Although our model can include the elastic energy associated with the lattice mismatch between precipitates and matrix, we ignore it in this paper in order to examine the effect of chemical free energy approximations on predicted growth kinetics of precipitates. In simulations, the interfacial energies and diffusivity were taken from first-principles calculations and experimental data, respectively. Six sets of chemical free energies were constructed in order to study the effect of the approximation in chemical free energies on the predicted growth of θ' precipitates in one and two dimensions.

2. Phase-field model

2.1. Description of microstructures

According to the orientation relationship $(100)_{\theta'} \parallel (100)_{\text{matrix}}$ and $(010)_{\theta'} \parallel (010)_{\text{matrix}}$, there exist three orientational variants of θ' precipitates [5,6]. Fig. 1 shows one of three θ' orientation variants, which has a broad interface with normal direction $\boldsymbol{n}$ along $\langle 001 \rangle$. In order to describe the θ' precipitation in the fcc α Al–Cu solid solution, we use four field variables, i.e. composition field $c(\boldsymbol{x}, t)$ associated with Cu composition and three order parameter fields $\eta_i(\boldsymbol{x}, t)(i = 1, 2, 3)$ associated with three θ' orientation variants. The order parameter $\eta_i(\boldsymbol{x}, t)$ is defined as 1 in the θ' phase and 0 in the α phase. It varies smoothly from 1 to 0 across the interface between θ' and α phases.

With the chemical free energies $f^{\alpha}(c_{\alpha}, T)$ and $f^{\theta'}(c_{\theta'}, T)$ of α and θ' phases, the chemical free energy of the system is defined as:

$$\begin{aligned} G(c, \eta_1, \eta_2, \eta_3, T) = {} & (1 - h(\eta_1, \eta_2, \eta_3))\, f^{\alpha}(c_{\alpha}, T) \\ & + h(\eta_1, \eta_{2,}\eta_3) f^{\theta'}(c_{\theta'}, T) \\ & + w g(\eta_1, \eta_2, \eta_3), \end{aligned} \tag{1}$$

where c_{α} and $c_{\theta'}$ are the molar fractions of Cu atoms in α and θ' phases respectively, T the absolute temperature, $g(\eta_1, \eta_2, \eta_3)$ a double-well potential, w the height of the double well potential, and $h(\eta_1, \eta_2, \eta_3)$ a monotonous function from 0 to 1. In the present paper, $g(\eta_1, \eta_2, \eta_3)$ and $h(\eta_1, \eta_2, \eta_3)$ are taken as:

$$h(\eta_1, \eta_2, \eta_3) = 3(\eta_1^2 + \eta_2^2 + \eta_3^2) - 2(\eta_1^3 + \eta_2^3 + \eta_3^3)$$

$$\begin{aligned} g((\eta_1, \eta_2, \eta_3)) = {} & (\eta_1^2 + \eta_2^2 + \eta_3^2) - 2(\eta_1^3 + \eta_2^3 + \eta_3^3) \\ & + (\eta_1^4 + \eta_2^4 + \eta_3^4) + (\eta_1^2\eta_2^2 + \eta_3^2\eta_1^2 + \eta_2^2\eta_3^2) \\ & + \eta_1^2(\eta_2^4 + \eta_3^4) + \eta_2^2(\eta_1^4 + \eta_3^4) \\ & + \eta_3^2(\eta_2^4 + \eta_1^4) + \eta_1^2\eta_2^2\eta_3^2. \end{aligned} \tag{2}$$

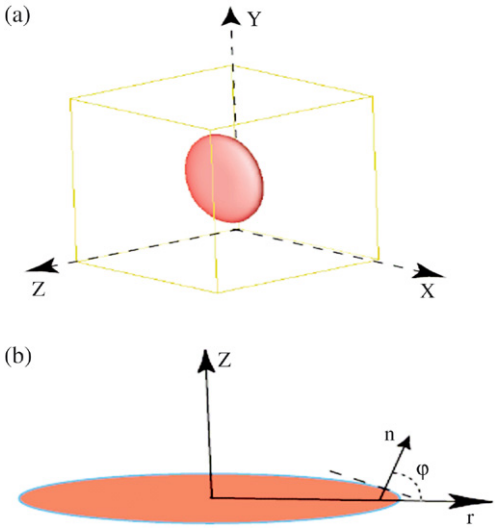

Fig. 1. (a) Coordinate system associated with θ', (b) definition of φ which is used to describe the interfacial energy and mobility anisotropies. n is the normal direction of the interface, and the angle φ is defined by $\varphi = \pi/2 - \arccos(n \cdot \langle 001 \rangle)$.

The total free energy $F(c, \eta_i, T)$ of the system includes chemical free energy and interfacial energy. It is defined as:

$$\begin{aligned} F(c, \eta_1, \eta_2, \eta_3, T) = \int_V \Bigg[& \frac{1}{\Omega_0} G(c, \eta_1, \eta_2, \eta_3, T) \\ & + \sum_{i=1}^{3} \frac{k^2(\varphi_i)}{2} |\nabla \eta_i|^2 \Bigg] \mathrm{d}V \end{aligned} \tag{3}$$

where Ω_0 is the molar volume, $\kappa(\varphi_i)$ is a gradient coefficient associated with anisotropic interfacial energy, and φ_i is the angle as shown in Fig. 1.

2.2. Kinetic equations

In the framework of phase-field models, the temporal and spatial evolution of conserved fields such as composition c is governed by the Cahn–Hilliard equation [16], whereas the evolution of non-conserved fields, such as order parameter η, is governed by the Allen–Cahn equation [17]

$$\begin{aligned} \frac{\partial c}{\partial t} &= \nabla \cdot \left[\frac{D(\eta_1, \eta_{2,}\eta_3, T)}{G_{cc}} \nabla \left(\frac{\partial G}{\partial c} \right) \right] \\ &= \nabla \cdot \left[M(\eta_1, \eta_{2,}\eta_3, T) \nabla \left(\frac{\partial G}{\partial c} \right) \right] \end{aligned} \tag{4}$$

$$\begin{aligned} \frac{\partial \eta_i}{\partial t} &= -L(\varphi_i) \frac{\delta F}{\delta \eta_i} \\ &= \frac{L(\varphi_i)}{\Omega_0} \left[-\frac{\partial G}{\partial \eta_i} - \Omega_0 \frac{\partial}{\partial \eta_i} \left(\frac{\kappa(\varphi_i)^2}{2} |\nabla \eta_i|^2 \right) \right] \end{aligned} \tag{5}$$

where $D(\eta_1, \eta_2, \eta_3, T)$ and $M(\eta_1, \eta_2, \eta_3, T)$ are chemical diffusivity and mobility, respectively, $L(\varphi_i)$ is the interface mobility coefficient, and G_{cc} is the second derivative of G with respect to the composition c.

We consider the interfacial region to be a mixture of α and θ' phases with the same chemical potential, i.e. c_{α} and $c_{\theta'}$ satisfy

the following set of constraint conditions,

$$c = [1 - h(\eta_1, \eta_2, \eta_3)]\, c_\alpha + h(\eta_1, \eta_2, \eta_3)\, c_{\theta'} \quad \text{and}$$
$$\frac{\partial f^\alpha(c_\alpha)}{\partial c_\alpha} = \frac{\partial f^{\theta'}(c_{\theta'})}{\partial c_{\theta'}}. \tag{6}$$

In order to simplify the evolution equations, let us consider an isolated precipitate. In this case, only two field variables are needed to describe the system, i.e. one composition field $c(\boldsymbol{x}, t)$ and one order parameter field η. Setting $\eta_1 = \eta_2 = 0$, $\eta_3 = \eta$ and $\varphi_3 = \varphi$, the evolution equations (4) and (5), are simplified as:

$$\frac{\partial c}{\partial t} = \nabla \cdot \left[\frac{D(\eta, T)}{G_{cc}}(G_{c\eta}\nabla\eta + G_{cc}\nabla c)\right] = \nabla \cdot [M(\eta, T)(G_{c\eta}\nabla\eta + G_{cc}\nabla c)] \tag{7}$$

$$\frac{\partial \eta}{\partial t} = \frac{L(\varphi)}{\Omega_0}\left[-\Omega_0 \frac{\partial}{\partial \eta}\left(\frac{\kappa(\varphi)^2}{2}|\nabla\eta|^2\right) + h'(\eta) \times \left[f^\alpha(c_\alpha) - f^{\theta'}(c'_\theta) - (c_\alpha - c'_\theta)\frac{\partial f^\alpha(c_\alpha)}{\partial c_\alpha}\right] - w g'(\eta)\right] \tag{8}$$

and the constraint conditions become,

$$c = [1 - h(\eta)]\, c_\alpha + h(\eta) c'_\theta \tag{9a}$$
$$\frac{\partial f^\alpha(c_\alpha)}{\partial c_\alpha} = \frac{\partial f^{\theta'}(c'_\theta)}{\partial c'_\theta} \tag{9b}$$

where $G_{c\eta}$ is the second derivative of G with respect to composition c and order parameter η. $h'(\eta)$ and $g'(\eta)$ are the first derivatives with respect to η.

In summary, the simulation of θ' precipitation reduces the solution of the kinetic equations (7) and (8) under the constraint conditions (9).

2.3. Chemical free energies

Murray [18] gave a critical assessment of the phase equilibria of the Al–Cu alloys based on optimization of experimental phase diagram and thermodynamic data. Not only the stable equilibrium diagram but also metastable and constrained equilibrium were predicted. The chemical free energies of α and θ' phases were

$$\begin{aligned} f^\alpha(c_\alpha, T) = {} & RT[c_\alpha \ln(c_\alpha) + (1 - c_\alpha)\ln(1 - c_\alpha)] \\ & + c_\alpha(1 - c_\alpha)[(-24085 - 18.18944T) \\ & + (40399.8 - 3.91235T)(1 - 2c_\alpha) \\ & + (-19683 + 16.06993T) \\ & \times(-1 + 3(1 - 2c_\alpha)^2)/2] \quad [\text{J/mol}] \end{aligned} \tag{10}$$

$$f^{\theta'}(c'_\theta, T) = -10245.8 + 0.0579T \quad [\text{J/mol}] \tag{11}$$

with fcc Al and fcc Cu being the reference states at corresponding temperatures. The chemical free energies versus the Cu composition are plotted in Fig. 2 for $T = 498$ K. Since θ' phase is considered as a stoichiometric compound, its chemical free energy is defined at one point $c_{\theta'} = 1/3$.

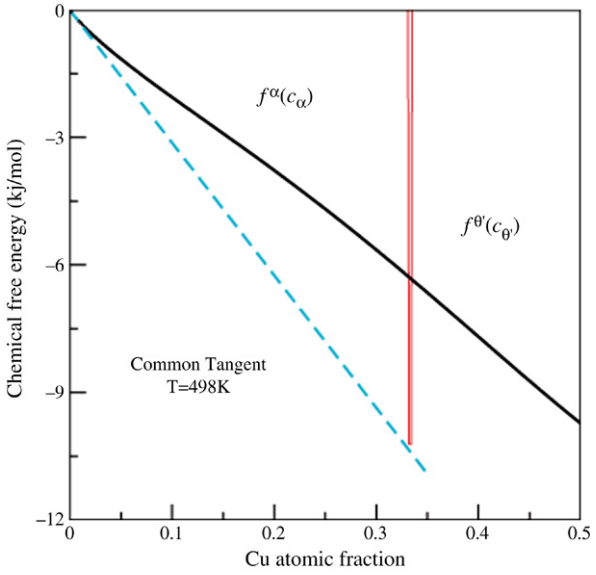

Fig. 2. Chemical free energies of α and θ' phases calculated from Eqs. (10) and (11) at Al rich compositions.

2.4. Model parameters

There are three unknown model parameters in the evolution equations (7) and (8), i.e. $L(\varphi)$, $\kappa(\varphi)$ and w which relate to materials constants such as interface mobility $\bar{L}(\varphi)$, interface thickness $2\lambda(\varphi)$ and interface energy $\sigma(\varphi)$. For a quantitative simulation, we must establish the relationships between these model parameters and material constants. Analyzing the equilibrium properties of kinetic equations (7) and (8) via thin interface limit analysis [19], the relationship among $\kappa(\varphi)$, w, $2\lambda(\varphi)$ and $\sigma(\varphi)$ can be obtained,

$$\sigma(\varphi) = \frac{\kappa(\varphi)\sqrt{w/\Omega_0}}{3\sqrt{2}} \tag{12}$$

$$2\lambda(\varphi) = \alpha\sqrt{2}\frac{\kappa(\varphi)}{\sqrt{w/\Omega_0}} \tag{13}$$

where α is a constant which depends on the definition of the interface. For example, when the interface is defined in the region between $\eta = 0.1$ and $\eta = 0.9$, then $\alpha = 2.2$. Following the same procedure, the relationship between $L(\varphi)$ and $\bar{L}(\varphi)$ can be established if the Peclet number, $p = 2\lambda V/\tilde{D}$ is very small ($\tilde{D}$ is the average interface diffusivity, and V is the interface velocity)

$$\frac{1}{\bar{L}(\varphi)} = \frac{1}{L(\varphi)}\int_{-\lambda}^{\lambda}\left(\frac{\mathrm{d}\eta}{\mathrm{d}x}\right)^2 \mathrm{d}x + \frac{c^e_\alpha - c^e_{\theta'}}{\Omega_0} \times \int_1^0 \left(\int_\lambda^x \frac{G_{cc}}{D(\eta)}[c(x) - c^{\mathrm{int}}_{\theta'}]\mathrm{d}x\right) h'(\eta)\mathrm{d}\eta \tag{14}$$

where $c^e_{\theta'}$ and c^e_α are equilibrium compositions in θ' and α phases respectively, and $c^{\mathrm{int}}_{\theta'}$ is the composition of θ' phase at the interface $x = \lambda$. Note that generally speaking, if the interface mobility $\bar{L}(\varphi)$ is known, the interface mobility coefficient

$L(\varphi)$ can be calculated by Eq. (14). Unfortunately, there are no experimental data available. Therefore, in the simulations, interfacial mobility coefficients are determined numerically.

2.5. Anisotropy of interfacial energy and interface mobility

The interfacial energies from first-principles calculation at 0 K for coherent and semi-coherent interfaces are 0.235 J/m^2 and 0.615 J/m^2 [19]. However, based on the theoretical estimation of the interfacial energy, Laird and Aaronson suggested that coherent and semi-coherent interfaces are about 0.03 J/m^2 and 0.35 J/m^2 [4]. Despite quantitative discrepancy, both calculations show that θ' precipitates have strong interface energy anisotropy. Two methods are often used to describe the dependence of interfacial energy on the interface normal in phase-field models [20–23]. One is to make the square-root of the gradient coefficient have the same directional dependence as the interfacial energy. Another method is to add higher order gradient energy terms. In the present work, the first method is used. We assume that the interfacial energy of plate-like θ' precipitate has cylindrical symmetry. It is described in terms of φ as:

$$\sigma(\varphi) = \frac{\sigma_0}{1+\gamma}\begin{cases} 1+\gamma_1+\gamma_2\sin(\varphi), \\ \quad -\pi/2 \le \varphi \le -\pi/2+\varphi_0 \\ 1+\gamma\cos(\varphi), \\ \quad -\pi/2+\varphi_0 \le \varphi \le \pi/2-\varphi_0 \\ 1+\gamma_1-\gamma_2\sin(\varphi), \\ \quad \pi/2\varphi_0 \le \varphi \le \pi/2 \end{cases} \tag{15}$$

where σ_0 is the interfacial energy at $\varphi = 0$, $\gamma_1 = \gamma\cos(\varphi_0)/\sin(\varphi_0)$, $\gamma_2 = \gamma/\sin(\varphi_0)$, γ is determined by the interfacial energy at $\varphi = \pi/2$. $\varphi_0 = \pi/200$ is chosen as a very small angle to describe two cusps at $\varphi = \pm\pi/2$ [24], which reflect two flat interfaces of θ' precipitates according to the Wulff Construction [25]. The gradient coefficient $\kappa(\varphi)$ is determined by Eq. (12) for given interfacial energy $\sigma(\varphi)$.

Since we have no experimental data on the interface mobility $\bar{L}(\varphi)$, we give the interface mobility coefficient $L(\varphi)$ the same angular dependence as $\sigma(\varphi)$

$$L(\varphi) = \frac{L_0}{1+\beta}\begin{cases} 1+\beta_2+\beta_1\sin(\varphi), \\ \quad -\pi/2 \le \varphi \le -\pi/2+\varphi_0 \\ 1+\beta\cos(\varphi), \\ \quad -\pi/2+\varphi_0 \le \varphi \le -\pi/2-\varphi_0 \\ 1+\beta_2-\beta_1\sin(\varphi), \\ \quad pi/2\varphi_0 \le \varphi \le \pi/2 \end{cases} \tag{16}$$

where L_0 is the interface mobility coefficient at $\varphi = 0$, $\beta_1 = \beta\cos(\varphi_0)/\sin(\varphi_0)$, $\beta_2 = \beta/\sin(\varphi_0)$, β is determined by the interface mobility at $\varphi = \pi/2$, and φ_0 is again taken to be $\pi/200$.

3. Dimensionless kinetic equations and input data

Using dimensionless variables $t^* = D_0 t/l^2$ and $x^* = x/l$ where l represents the grid spacing (Δx) or the characteristic length, the kinetic equations (7) and (8) are simplified to:

$$\frac{\partial\eta}{\partial t^*} = L^*(\varphi)\left\{\nabla^*\cdot\kappa^*(\varphi)^2\nabla^*\eta + h'(\eta)\left[f^{\alpha*}(c_\alpha) - f^{\theta'*}(c'_\theta) - (c_\alpha - c'_\theta)\frac{\partial f^{\alpha*}(c_\alpha)}{\partial c_\alpha}\right] - w^* g'(\eta)\right\} \tag{17}$$

$$\frac{\partial c}{\partial t^*} = \nabla^*\cdot(D^*(T)\nabla^* c) + \nabla^*\cdot(D^*(T)h'(\eta)(c_\alpha - c_{\theta'})\nabla^*\eta) \tag{18}$$

where:

$$L^*(\varphi) = \frac{L(\varphi)C_{44}l^2}{D_0}; \qquad \kappa^*(\varphi)^2 = \frac{\kappa(\varphi)}{C_{44}l^2};$$

$$f^{\alpha*}(c_\alpha) = \frac{f^\alpha(c_\alpha)}{C_{44}\Omega_0}, \qquad f^{\theta'*}(c_{\theta'}) = \frac{f^{\theta'}(c_{\theta'})}{C_{44}\Omega_0};$$

$$w^* = \frac{w}{C_{44}\Omega_0}; \qquad D^*(T) = \frac{D(T)}{D_0}, \qquad \nabla^* = \frac{\nabla}{l}.$$

Periodic boundary conditions in x-, y- and z-directions are used and the kinetic equations are solved numerically using the Fourier-spectral method [26]. The input data include the grid spacing $\Delta x = 0.5$ nm, the semi-coherent interface thickness $2\lambda_1 = 6\Delta x = 3$ nm, the constant $\alpha = 2.2$ in Eq. (13), the molar volume $\Omega_0 = 10^{-5}$ m^3/mol, coherent interfacial energies (0.235 J/m^2) and semi-coherent interfacial energy (0.615 J/m^2). We assume that the diffusion coefficient $D(\eta, T)$ only depends on temperature T [27],

$$D(T) = D_0\exp\left[-\frac{Q}{RT}\right] \tag{19}$$

where $D_0 = 4.5\times10^{-5}$ m^2/s, $Q = 1.33\times10^5$ J/mol, and R is the universal gas constant. The overall composition and aging temperature to be simulated are $c_0 = 0.0172$, i.e. 4 wt % Cu, and $T = 498$ K. The composition is that for which we have the most experimental, and the temperature is one for which only θ' precipitates (not GP zones or θ'') are observed. In our model, once the interfacial energy and interface thickness and artificial double well potential height w^* are given, the model parameter k^* is uniquely determined, independent of the chemical free energies unlike the WMB model [28]. We can now make a comparison of the effect of different chemical free energy approximations on calculated precipitate growth kinetics.

4. Results and discussion

In order to study the effect of the approximation in chemical free energies on the calculated growth kinetics, six sets of chemical free energies $f^\alpha(c_\alpha, T)$ and $f^{\theta'}(c_{\theta'}, T)$ are constructed. They are numbered Case # (# = 0, 1, . . . , and 5), and plotted in Fig. 3. In Case 0, the chemical free energy of stoichiometric line compound θ' phase is employed. In order to avoid multiple solutions of the constraint equation (10), the convex part of $f^\alpha(c_\alpha, T)$ is smoothly replaced by a concave function, that is

$$\tilde{f}^\alpha(c_\alpha, T) = \begin{cases} f^\alpha(c_\alpha, T) & c_\alpha \le c^* \\ A_0 + A_1 c_\alpha & c_\alpha \ge c^* \end{cases}$$

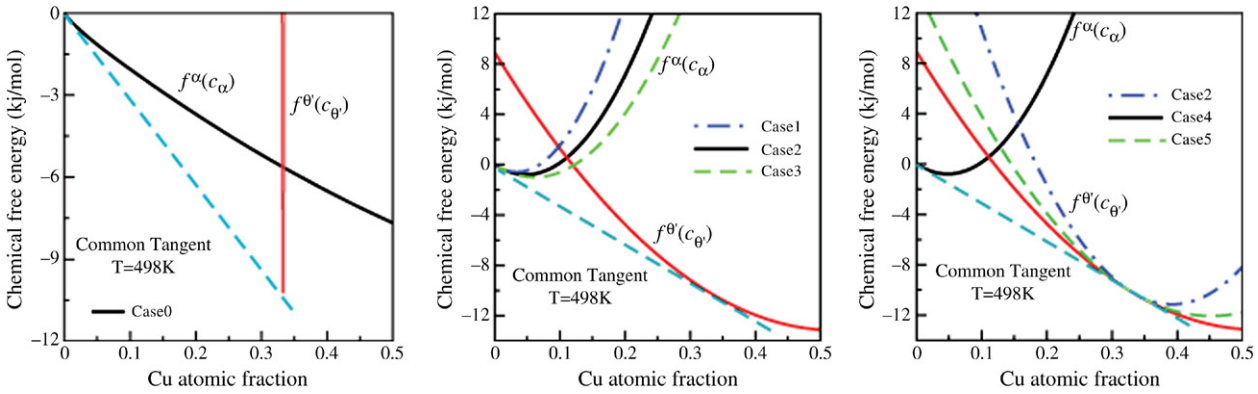

Fig. 3. Six sets of chemical free energies of α and θ' phases.

Table 1
Driving forces of phase transformation and nucleation for approximated chemical free energies at $T = 498$ K

Cases	$\Delta\tilde{G}_p$ (J/mol) transformation	$\Delta\tilde{G}_n$ (J/mol) nucleation
1	−103	−4568
2, 4 and 5	−72	−3187
3	−55	−2456
0	−72	−2484

where c^* is the spinodal composition, i.e., the small root of $\frac{\partial^2 f^{\alpha}(c_{\alpha},T)}{\partial^2 c_{\alpha}} = 0$, A_0 and A_1 are determined by the values of function $f^{\alpha}(c_{\alpha}, T)$ and its first derivative at $c_{\alpha} = c^*$. In Case 1 to Case 5, $f^{\alpha}(c_{\alpha}, T)$ and $f^{\theta'}(c_{\theta'}, T)$ are approximated with parabolic functions that give the same common tangent as the CALPHAD type functions (10) and (11), but have different second derivatives at the equilibrium phase compositions. Table 1 shows nucleation driving force $\Delta\tilde{G}_n$ and phase transformation driving force $\Delta\tilde{G}_p$ for different approximations. The second derivative in Case 2, is fitted by minimizing the difference in transformation driving forces at the overall composition $c_0 = 0.0172$ with respect to the analytical free energy (10). The chemical free energy in Case 3 is fitted by minimizing the difference in nucleation driving forces with respect to the analytical free energies (10) and (11).

4.1. Determination of interface mobility coefficient

For a given semi-coherent interface energy (0.615 J/m^2), interface thickness ($6\Delta x$), and set of chemical free energies, the interface mobility coefficient L^* is the only unknown parameter. There are no experimental data available. Therefore, it is important to examine this parameter numerically. To do so, one-dimensional growth of θ' precipitate is simulated with a θ' precipitate of a size of $40\Delta x$ placed in the centre of a simulation cell $2048\Delta x$. The initial composition is set to be the equilibrium composition $c = 0.33$ in the precipitate and $c_0 = 0.0172$ in the matrix (α phase). Fig. 4 presents the precipitate length as a function of time and square root of time, calculated using the free energies of Case 2 and various values of the interface mobility coefficient L^*. From Fig. 4, it can be seen

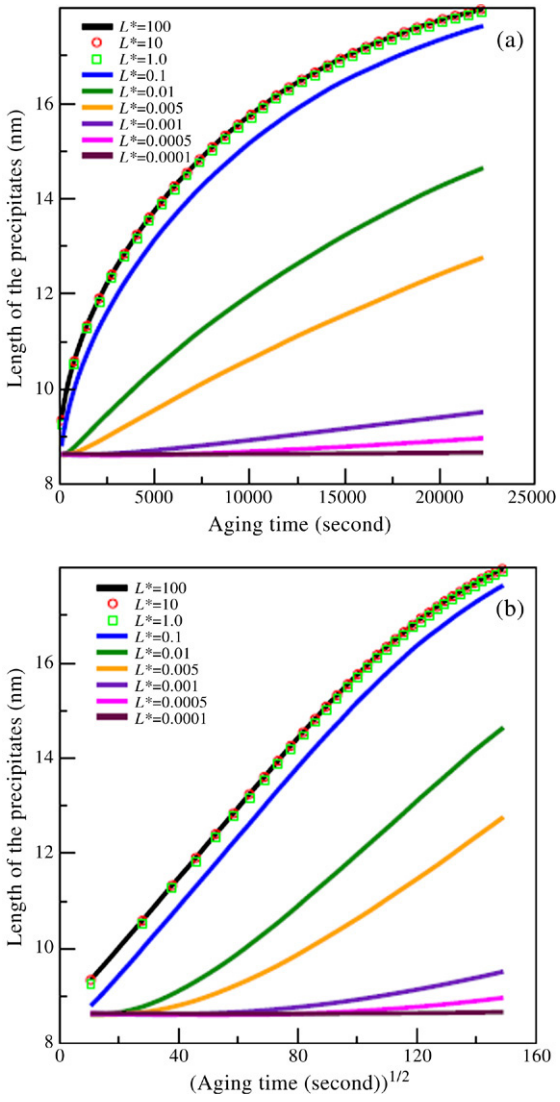

Fig. 4. Precipitate length as a function of time t, (a) vs t and (b) vs $\sqrt{t}$.

that the relationship between the precipitate length and time approaches to be linear as L^*decreases while the relationship between the length and square root of time approaches to be linear as L^* increases. The nonlinear relationship observed in

Fig. 4(b) for large L^* and long time is due to the periodic boundary conditions. Two critical values of L^* are determined, i.e., $L^* = 0.001$ and 0.1. When $L^* < \sim 0.001$ the growth is interface-controlled and when $L^* > \sim 0.1$ it is diffusion-controlled. The results also show that the two critical values are independent of chemical free energies, i.e. they are the same for all six sets of chemical free energies.

The above results illustrate that the developed model is able to describe interface-controlled and diffusion-controlled growth as well as mix-controlled growth depending on the value of interface mobility coefficient L^*. In the present work, we are interested in studying the effect of chemical free energy approximations on diffusion-controlled growths of precipitates. Therefore, a large interface mobility coefficient $L^* = 50$ is employed in the following simulations. In addition, we consider two cases: constant diffusivity and constant mobility, i.e. either the D or M in Eq. (4) is assumed to be constant.

4.2. Diffusion-controlled growth in 1D

4.2.1. Constant diffusivity

Using the simulation cell described in last section, one dimensional growth of θ' is simulated with six different chemical free energies. Fig. 5(a) shows the composition evolution for chemical free energy Case 0–3. As expected, one-dimensional diffusion-controlled growth at constant diffusivity is independent of chemical free energies. The growth is completely driven by the composition gradient, which can be seen from the Eq. (4). In this case, an analytic solution can be found [29].

$$c(\boldsymbol{x}, t) = c_0 + (c_\alpha^e - c_0)\mathrm{erfc}\left(\frac{x - x_{\mathrm{int}}}{2\sqrt{Dt}}\right) \tag{20}$$

$$v = \frac{\mathrm{d}x_{\mathrm{int}}}{\mathrm{d}t} = \frac{c_\alpha^e c_0}{c_\alpha^e - c_{\theta'}^e}\sqrt{\frac{D}{\pi t}} \tag{21}$$

where x_{int} is the interface position, v the velocity of interface migration and c_0 the overall composition. It is found that the simulated composition profiles are in good agreement with the analytical solution except at the interface region because the analytical solution has a sharp interface. The interface velocities calculated by Eq. (21) and simulated with different chemical free energies are presented in Fig. 5(b). Except at long times, the phase-field simulations exactly reproduce the analytical solution. The deviation in interface velocities at late stage is due to the periodic boundary conditions in the simulations which differ from the analytical solution with constant composition c_0 at infinite.

4.2.2. Constant mobility

Now let us consider the growth with constant mobility. With the assumption of constant mobility, the Eq. (4) can be rewritten as:

$$\frac{\partial c}{\partial t} = \nabla \cdot (M_0 G_{cc} \nabla c) = M_0 \nabla \cdot (G_{cc} \nabla c) \tag{22}$$

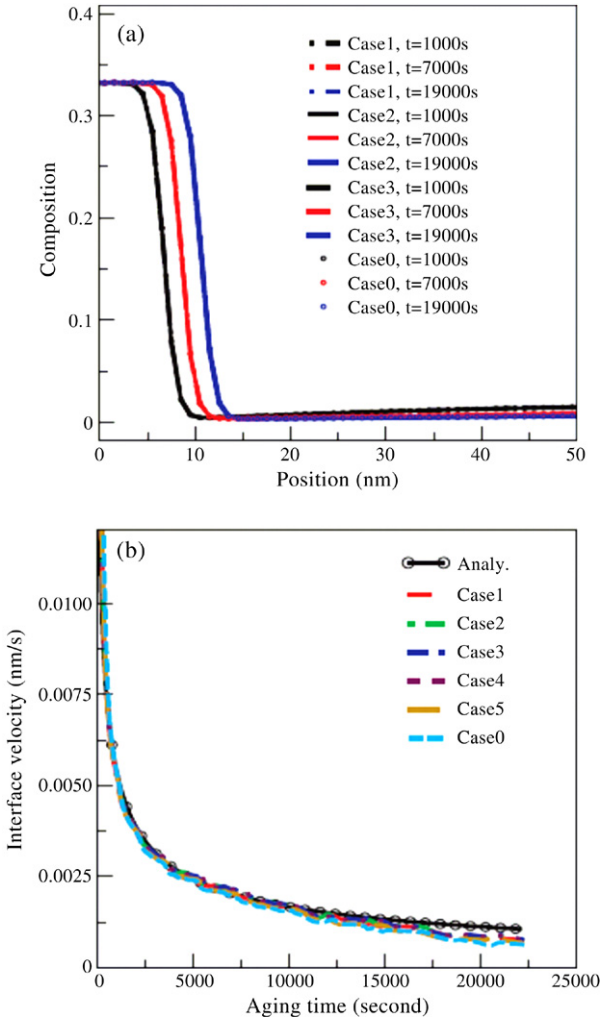

Fig. 5. (a) Composition profile evolution. The profiles overlap at a given time for different chemical free energies, (b) Comparison of interface velocities obtained by the phase-field simulations with different chemical free energies and analytical solutions.

where

$$G_{cc} = \frac{f^{\alpha}_{c_\alpha c_\alpha} f^{\theta'}_{c_{\theta'} c_{\theta'}}}{h(\eta) f^{\alpha}_{c_\alpha c_\alpha}(c_\alpha, T) + (1 - h(\eta)) f^{\theta'}_{c_{\theta'} c_{\theta'}}(c_{\theta'}, T)}.$$

Since $h(\eta)$ changes from 1 in the θ' phase to 0 in the α phase, the constant mobility implies that the diffusivity changes continuously from $M_0 f^{\theta'}_{c_{\theta'} c_{\theta'}}$ in the θ' to $M_0 f^{\alpha}_{c_\alpha c_\alpha}$ in the α phase. Fig. 6(a)–(b) presents the composition evolution for six different chemical free energies. It is seen in Fig. 6(b) that different parabolic approximations of θ' free energy give almost the same growth kinetics, but that different approximations for α do affect the calculation. From Case 1 to Case 3, the second derivative $f^{\alpha}_{c_\alpha c_\alpha}$ decreases. This means that the overall driving force or effective diffusivity decreases from chemical free energy Case 1–3. We find that the θ' growth kinetics strongly depends on the chemical free energy of solid solution phase. It is a natural result that the larger the driving force is, the faster the precipitate grows as shown in Fig. 6(a). Fig. 6(a) also show another interesting fact that the chemical free energy

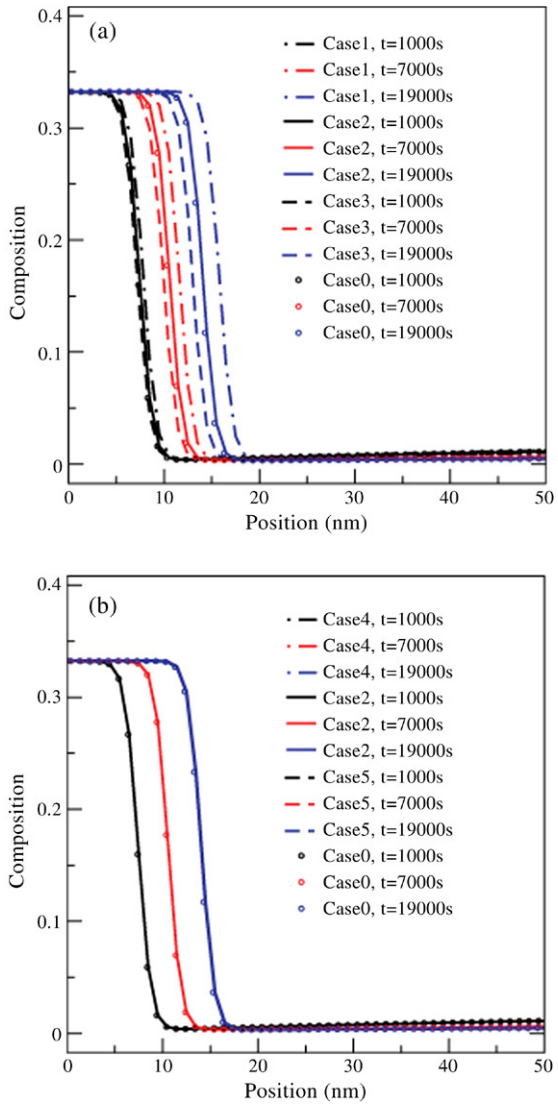

Fig. 6. (a) Composition profile evolution for chemical free energy Case 0–3, (b) composition profile evolution for chemical free energy Case 2, Case 4 and Case 5, where the profiles overlap at a given time for different chemical free energies.

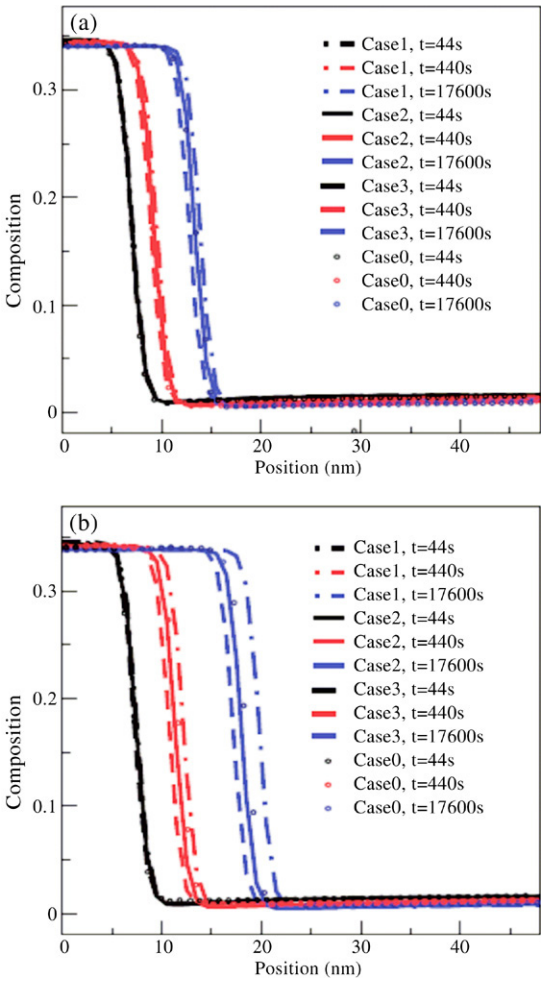

Fig. 7. (a) Composition profile evolution with constant diffusivity, (b) composition profile evolution with constant mobility.

Case 0 and Case 2 provide a very similar growth kinetics. Case 0 is the real chemical free energy described by Eq. (10) except the convex part while Case 2 is fitted by the overall phase transition driving force at c_0. Therefore, from one-dimensional simulations, we can conclude that (1) to minimize the effect of chemical free energy approximation on growth kinetics the parabolic function of solid solution phase should be fitted by the overall phase transformation driving force; (2) the chemical free energy of stoichiometric compound phase can be approximated by a parabolic function which does not significantly affect its growth kinetics.

4.3. Diffusion-controlled growth of a circular precipitate in 2D

4.3.1. Constant diffusivity and constant mobility

A one-dimensional precipitate has a planar interface. Now we consider the growth of a circular precipitate in two dimensions with a curved interface. The curved interface raises the free energy of the precipitate phase relative to a planar interface due to the Gibbs Thomson effect. Consequently, the equilibrium compositions at the phase interface between the precipitate and matrix will change during the growth. In the simulations, a circular θ' precipitate with radius $a = 12\Delta x$ is initially placed in the centre of the simulation cell $512\Delta x \times 512\Delta x$. The initial composition in the precipitate and the matrix are $c = 0.33$ and $c_0 = 0.0172$. Fig. 7(a)–(b) show the composition profiles along the radial direction of the circular precipitate for various cases and time. We can see that different chemical free energies (Case 0–3) affect the circular precipitate growth in both constant diffusivity and constant mobility. The results in Fig. 7 illustrate that the effect of curved interface and chemical free energy approximations on growth kinetics is smaller with constant diffusivity than that with constant mobility. From the results in Fig. 8, we can drawn the same conclusion as in Section 4.1 that the chemical free energy of stoichiometric compound phase can be approximated by a parabolic function, and chemical free energy Case 2 is the best approximation for the solid solution because it produces the same result as chemical free energy Case 0.

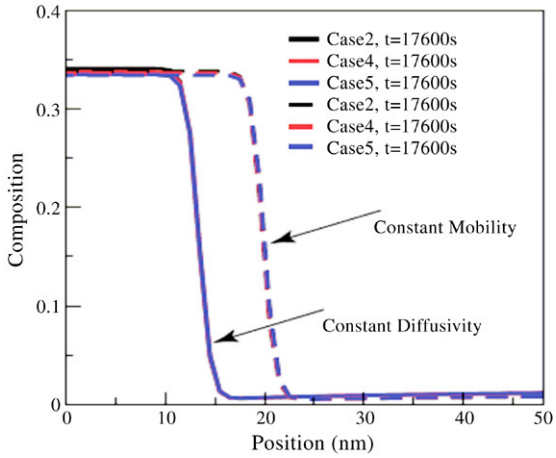

Fig. 8. Composition profile evolutions with constant diffusivity and mobility. The composition profiles overlap for different chemical free energies for constant diffusivity and mobility, respectively.

4.3.2. Growth kinetics of θ' in 2D

Plate-like θ' precipitates have strong anisotropies in interfacial energy and interface mobility. To study the effect of the approximations in chemical free energies on the growth kinetics, we assume that the lengthening of the plate-like precipitate is diffusion-controlled while the thickening is a mixture of diffusion and interface controlled growth. In the simulations, parameters $\beta = 10\,000$, $L_0^* = 50$, $\sigma_0 = 0.615\ \mathrm{J/m^2}$ and $\gamma = 2$ are used. The interface mobility and interfacial energy anisotropy are described by Eqs. (16) and (17). We thus obtain the interface mobility coefficient and interfacial energy of the planar precipitate interface at $\varphi = \pm\pi/2$ as $L^* = 0.005$ and $\sigma_0 = 0.205\ \mathrm{J/m^2}$. In order to eliminate the effect of grid numerical pinning in z direction, a small grid size is used, i.e. $\Delta z = 0.333\Delta x$. In addition, although the more accurate chemical free energy Case 0 can still be used in simulating plate-like precipitate growth, numerical stability requires that much smaller grid size and time step be used for simulating the growth of a very thin θ' precipitate (few nanometer thickness). Therefore, we only use the five sets of chemical free energies (Case 1–5) in this section. We put an elliptic θ' precipitate with a long axis $a = 12\Delta x$ and a short axes $b = 4\Delta z$ in the centre of the simulation cell $512\Delta x \times 512\Delta z$. The composition in the precipitate and the matrix are $c = 0.33$ and $c_0 = 0.0172$, respectively. Fig. 9(a)–(b) shows the lengthening and thickening of θ' for constant diffusivity, and Fig. 10(a)–(b) for constant mobility. The results show the precipitate grows almost linearly with very slow thickening rates. If a smaller mobility of the planer interface, $L^* = 0.0002$, is used, constant thickness and exactly linear lengthening are observed. The linear lengthening is in agreement with the theoretical prediction under assumptions of diffusion-controlled growth and constant thickness [29]. It should be pointed out that the rapid increase of θ' thickness in the early stage is due to the relaxation of initial non-equilibrium elliptic precipitate. A detailed comparison with experimental lengthening and thickening data will be reported soon.

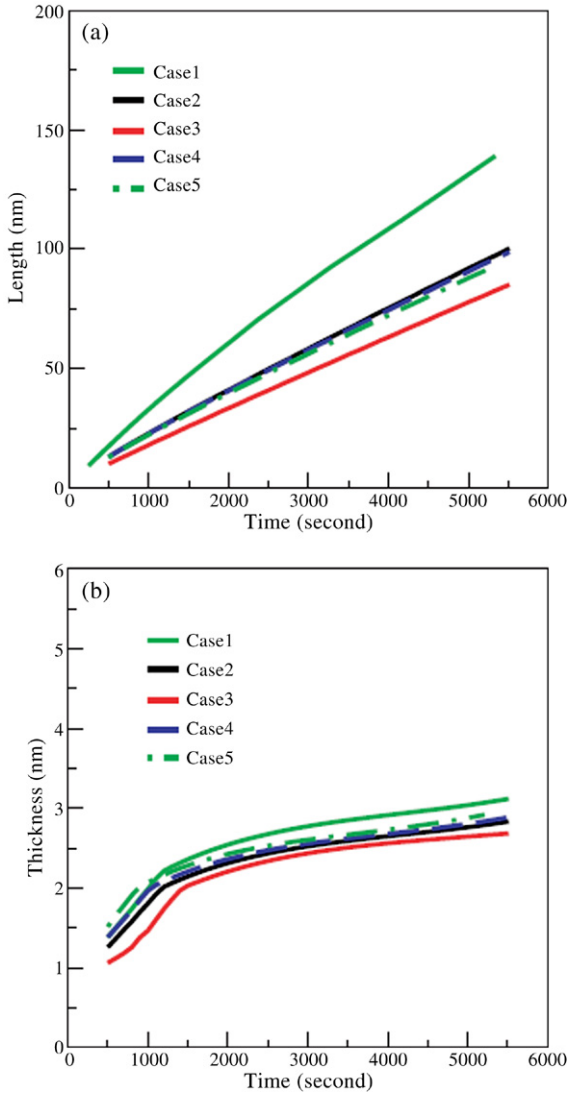

Fig. 9. (a) Lengthening with constant diffusivity, (b) thickening with constant diffusivity.

Fig. 9(a) shows a considerable increase of the lengthening rate of a plate-like precipitate from the chemical free energy Case 3, Case 2 to Case 1. A comparison between the results in Fig. 7(a) and Fig. 9(a) demonstrate that the lengthening of plate-like precipitates depends much more strongly on the chemical free energy of the solid solution phase than that of a circular precipitate. As we know, the Gibbs Thomson effect causes an increase in equilibrium compositions at interface. The increase of equilibrium compositions depends on the curvature of the interface and chemical free energy. For example, the equilibrium composition in the matrix side increases as the second derivative of the chemical free energy G_{cc} decreases from Case 1, Case 2 to Case 3. A lower equilibrium composition at the interface for Case 1 generates a larger diffusion driving force compared to Case 3. This explains why the lengthening increases with the increase of G_{cc} as shown in Fig. 9. To understand that the lengthening of plate-like precipitates depends much more strongly on the chemical free energy of the solid solution phase than that of a

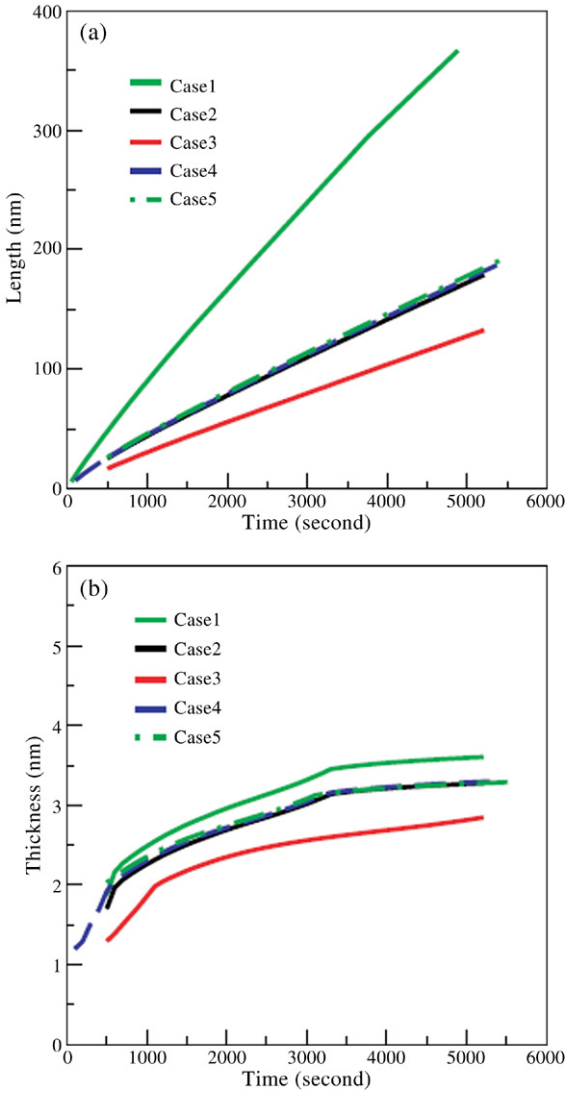

Fig. 10. (a) Lengthening with constant mobility, (b) thickening with constant mobility.

circular precipitate, we should consider the following fact. For a circular particle, the Gibbs Thomson effect is important only when the radius is small. It becomes increasingly less important as the particle size increases. As a result, the growth of the circular particle is insensitive to chemical free energy under the assumption of a constant diffusivity. For the plate-like θ', however, the radius at the rim is very small, about 2–4 nm, and remains almost constant during the growth. Therefore, the Gibbs–Thomson effect exists during the whole growth process. Therefore, we conclude that the strong dependence of growth kinetics on the free energy approximation of the solution phase is attributed to the Gibb's Thomson effect. In the case of constant mobility, besides the Gibbs Thomson effect, chemical free energies also affect the effective diffusivity in the solid solution phase. It is expected that the dependence of the lengthening on chemical free energy in the case of constant mobility is stronger than that in the case of constant diffusivity as shown in Fig. 10. In addition, we can see that both the lengthening and thickening are almost independent of the chemical free energy of the precipitate phase (Case 2, Case 4 and Case 5). This confirms again our conclusion that the parabolic approximation of θ' free energy does not affect the growth kinetics.

5. Conclusions

In this work, we studied the effect of free energy approximations on the precipitation kinetics of plate-like precipitates with strong anisotropies in interfacial energy and interface mobility. Simulation results showed that the phase-field model is able to reproduce the analytical solutions in one dimensional diffusion-controlled growth and the linear growth behaviour of plate precipitate with constant thickness, and to reproduce a reasonable lengthening and thickening of θ' precipitate in 4wt %Al–Cu alloys. Six sets of chemical free energies were constructed for studying the effect of chemical free energy approximations on calculated growth kinetics. The results demonstrated that (1) the chemical free energy of stoichiometric compounds can be reasonably approximated by a parabolic free energy function; (2) the precipitate growth kinetics is sensitive to the chemical free energy of solid solution phase. However, a parabolic function fitted by the overall phase transition driving force Case 2 is a reasonable approximation for the chemical free energy of solid solution phase; (3) for very thin precipitates such as θ' precipitates in Al–Cu alloys, the Gibbs Thomson effect enhances the effect of chemical free energy approximation on growth kinetics. This implies that an accurate chemical free energy is needed for a quantitative simulation of θ' precipitate growth kinetics. In addition, even though the simulations results showed that precipitate growth kinetics is insensitive to the free energy approximation for the precipitate phase, we would like to point out that the nucleation of θ' does depend strongly on the free energy functions used for the precipitate phase.

Acknowledgements

This work is supported by the US Department of Energy under Contract W-7405-ENG-36, the National Science Foundation Information Technology Research Project (NSF-ITR) and by Alcoa Inc.

References

[1] H.K. Hardy, J. Inst. Metals 79 (1951) 321.
[2] H.K. Hardy, J. Inst. Metals 82 (1953) 236.
[3] E. Hornbogen, Aluminium 43 (1967) 115.
[4] C. Laird, H.I. Aaronson, Trans. Metall. Soc. AIME 242 (1968) 1393.
[5] J.D. Boyd, R.B. Nicholson, Acta Metall. 19 (1971) 1379.
[6] P. Merle, F. Fouquet, Acta Mater. 29 (1981) 1929.
[7] R. Sankaran, C. Laird, Acta Metall. 22 (1974) 957.
[8] R. Wagner, R. Kampmann, in: R.W. Cahn, P. Haasen, E.J. Krammer (Eds.), Material Science and Technology, vol. 5, VCH, Weinheim, 1991, p. 246.
[9] L.F. Mondolfo, Aluminum Alloys: Structure and Properties, Butterworths, 1976.
[10] R.D. Doherty, in: R.W. Cahn, P. Hassen (Eds.), Physical Metallurgy, Elsevier Science, 1996.
[11] A.W. Zhu, J. Chen, E.A. Starke Jr., Acta Mater. 48 (2000) 2239.

[12] D.Y. Li, L.Q. Chen, Acta Mater. 46 (1998) 2573.
[13] V. Vaithyanathan, C. Wolverton, L.Q. Chen, Phys.Rev. Lett. 88 (2002) 125503.
[14] I. Steibach, F. Pezzolla, B. Nestler, M. Seebelberg, R. Prieler, G.J. Schmitz, J.L.L. Rezende, Physica D 94 (1996) 135.
[15] S.G. Kim, W.T. Kim, T. Suzuki, Phys. Rev. E 60 (1999) 7186.
[16] J.W. Cahn, Acta Metall. 9 (1961) 795.
[17] S.M. Allen, J.W. Cahn, J. Phys. C 7 (1977) C 7.
[18] J.L. Murray, Int. Metall. Rev. 30 (1985) 211.
[19] C. Wolverton, Phil. Mag. Lett. 79 (1999) 683.
[20] J.S. Langer, in: G. Grinstein, G. Mazenko (Eds.), Directions in Condensed Matter Physics, vol. 165, World Scientific, Singapore, 1986.
[21] J.E. Taylor, J.W. Cahn, Physica D 112 (1998) 381.
[22] T.A. Abinandanan, F. Haider, Philos. Mag. A 81 (2001) 2457.
[23] W. Dreyer, W.H. Muller, Bioceramics 240 (15) (2003) 901.
[24] I. Loginova, Phase-field modeling of diffusion controlled phase transformations, Ph.D. Thesis, Royal Institute of Technology, 2003.
[25] W.C. Johnson, C.L. White, P.E. Marth, P.K. Ruf, S.M. Tuominen, K.D. Wade, K.C. Russell, H.I. Aaronson, Metall. Trans. A 911 (1975).
[26] L.Q. Chen, J. Shen, Comput. Phys. Commun. 108 (1998) 147.
[27] H. Weiland (private communication).
[28] A.A. Wheeler, W.J. Boettinger, et al., Phys. Rev. A 45 (1992) 7424.
[29] D.A. Porter, K.E. Easterling, Phase Transitions in Metals and Alloys, Chapman & Hall, New York, 1992.